KSME

Springer

Journal of Mechanical Science and Technology 35 (2) 2021

Original Article
DOI 10.1007/s12206-021-0120-4

Keywords:
· Tri-screw pump
· Fluid-structure coupling
· Computational fluid dynamics
· Screw clearance
· Numerical simulation

Correspondence to:
Hongling Hou
xjtuhhl@163.com

Citation:
Zhao, Y., Zhu, B., Hou, H., Zhao, S. (2021). Performance analysis of embedded tri-screw pump based on computational fluid dynamics. Journal of Mechanical Science and Technology 35 (2) (2021) 601~614.
http://doi.org/10.1007/s12206-021-0120-4

Received July 17th, 2020
Revised September 14th, 2020
Accepted October 19th, 2020

† Recommended by Editor
Yang Na

Performance analysis of embedded tri-screw pump based on computational fluid dynamics

Yongqiang Zhao[1], Bowen Zhu[1], Hongling Hou[1,2] and Shengdun Zhao[1,3]

[1]School of Mechanical Engineering, Shaanxi University of Technology, Hanzhong, China, [2]School of Mechanical Precision Instrument of Engineering, Xi'an University of Technology, Xi'an, China, [3]School of Mechanical Engineering, Xi'an Jiaotong University, Xi'an, China

Abstract To meet the stringent size and noise requirements for hydraulic pumps used in submarines, an embedded tri-screw pump is proposed. The pump is embedded in the core of the servo motor to form a new servo motor pump. This paper first presents the embedded tri-screw pump, as well as the cross-section profile design and parameter equations of the driving and driven screws. Velocity and pressure field distributions as well as changes in internal pressure and shear stress inside the embedded tri-screw pump with different radial and inter-lobe clearances were investigated using computational fluid dynamics. Furthermore, screw deformation under multi-field coupling was analyzed. In contrast to torque or fluid pressure acting alone, under the fluid-solid coupling effect, screw deformation and stresses are inversely proportional to the rotational speed of the pump and directly proportional to the power and output pressure. The simulation and experimental results were consistent for various outlet pressures and rotational speeds. Radial clearance of the screw has a more significant influence on leakage than inter-lobe clearance and therefore, more impact on the volumetric efficiency of the pump.

1. Introduction

To meet the stringent requirements of submarine hydraulic pumps, which are typically installed in small spaces and must have both low noise and vibration characteristics, a new embedded tri-screw pump structure is proposed. The pump is embedded in the core of the servo motor to form a new type of motor pump. Tri-screw pumps and twin-screw pumps belong to the same category of screw pumps, and both offer outstanding advantages in terms of noise, vibration, and flow stability, compared with plunger pumps.

In studies on the internal flow field of screw pumps, the twin-screw pump is typically selected as the research object, then the flow field, pressure field, and velocity field of the pump are simulated [1, 2]. Flow characteristics of fluid in the pump and the formation of cavitation bubbles at various speeds and exhaust pressures have been analyzed [3]. Temperature and pressure distributions at multiple points of the screw have also been obtained by experiment, and the influence of screw deformation on the leakage and volumetric efficiency of the pump have been analyzed [4]. Furthermore, the heat-fluid-solid coupling method can be used to simulate mixed transportation processes of gases and liquids [5, 6].

Twin-screw compressors and extruders have a similar structure to the twin-screw pump, for which a three-dimensional transient fluid dynamic grid was previously established to improve simulation accuracy [7-9]. The maximum ball method and minimum section method can be used to calculate the gap between two matched screw rotors in order to determine the leakage path [10]. The influence of thermodynamic coupling of the screw and thermodynamic temperature changes of the compressed gas on the leakage gap have also been examined [11, 12]. Moreover, thermo-liquid coupling simulations of the rotor temperature of the twin-screw expander and thermal deformation of the rotor and casing have been performed [13, 14]. Steady-

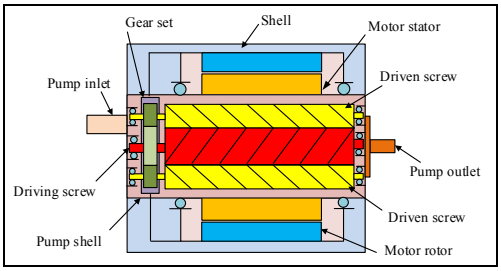

Fig. 1. Schematic drawing of embedded tri-screw pump.

state numerical simulations of the twin-screw kneader were previously carried out, and the influence of increasing rotor pitch or decreasing gap on the viscosity dissipation rate have been examined [15-17].

Research on the tri-screw pump has mainly focused on reducing wear and leakage and improving the manufacturing precision and reliability of the screw pump [18]. For instance, to slow down wear, ellipse and arc passivation methods for sharp edges of the pump screw sharp have been proposed [19-21]. To improve machining accuracy, the precision forming grinding method was used instead of the milling method for manufacturing screws used in the pump [22, 23].

Computational fluid dynamics (CFD) has been applied to study the internal flow fields of twin screw pumps and other similar pumps. However, CFD has never been used to study the flow characteristics of tri-screw pumps. The twin-screw pump is non-sealed, whereas the tri-screw pump is sealed, which results in large differences in the internal flow fields and working characteristics. Drawing on the previous success of computational fluid dynamics (CFD) models of the twin-screw pump, in this study, a simulation analysis and experimental research were carried out on the driving and driven screws of the embedded tri-screw pump. The maximum shear stress distribution of the pressure field and velocity field in the pump under various pressure differences and inter-lobe clearances, as well as their influence on volumetric efficiency, were studied. Finally, the relationship between the working load of the embedded tri-screw pump and the torque of the driving motor was investigated using a method for solving fluid-structure coupling problems and laws for deformation and stress distributions in the driving screw and driven screw were obtained.

2. Design and profile optimization of embedded tri-screw pump

2.1 Composition of embedded tri-screw pump system

The structure of the embedded tri-screw pump is comprised of a tri-screw pump, a permanent magnet synchronous motor, and a synchronous gear set, as illustrated in Fig. 1. The tri-screw pump can be embedded in the stator core of the outer-rotor permanent magnet synchronous motor and adopts a new axial flow structure with suction components on one end and discharge components on the other.

Table 1. Tooth profile curves of driving and driven screws.

Tooth profile curves	Driven screw	Tooth profile curves	Driving screw
ab	Arc	*a'b'*	Arc
bc	Long epicycloid	*b'c'*	Shortened epicycloid
cd	Arc	*c'd'*	Arc
de	Arc	*d'e'*	Arc

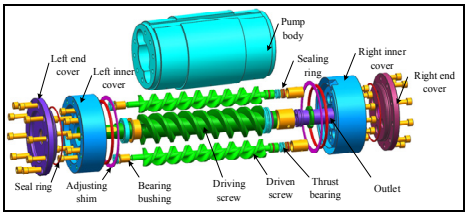

Fig. 2. Drawing of tri-screw pump structure.

The structure of the embedded tri-screw pump designed to improve upon the traditional tri-screw pump is shown in Fig. 2. The driving screw has a hollow structure, which forms the discharge channel of the pump and is connected to the outlet of the pump. The ends of the two driven screws are supported by bearing bushes and thrust bearings, which is different from the floating axial structure of the driven screw of the traditional tri-screw pump. Left and right inner covers are used to install the screw bearing and to balance the axial forces of the driving and driven screws.

2.2 Design and optimization of screw rotor profile

When the driving and driven screws of the tri-screw pump engage, the spiral groove is divided into several relatively closed cavities and the spiral surfaces of the driving and driven screws separate the sealed cavities. Therefore, the spiral surfaces of the screws must be tangent to one another; that is, the screw profile at the end face must meet the requirements of a continuous tangent. The end face curves of the driving and driven screws make up a pair of conjugate curves, and tangent points of the two curves move continuously from one end of the tooth profile to the other.

Since a cusp exists in the common tangent of the end profiles of the driving and driven screws, wear of the end profile easily occurs, reducing the screw life. Therefore, the end profile should be smooth. Optimal designs of the end profiles of the driving and driven screw rotor are considered in the next section. The tooth profile curves of the driving and driven screws are listed in Table 1.

2.2.1 Driven screw profile

The end profile of the driven screw rotor is shown in Fig. 3. The profile is mainly composed of four curves: tooth root arc *ab*, long epicycloid *bc*, modified arc *cd*, and tooth top arc *de*. A parametric equation can be defined for each curve.

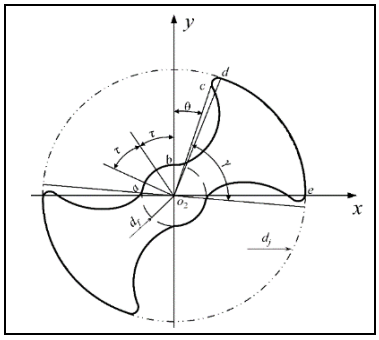

Fig. 3. Cross-sectional profile of driven screw.

(a) Arc *ab* forms part of the tooth root arc of the driven screw. The starting position is $\frac{\pi}{2}$ and the end position is $\frac{\pi}{2}+2\tau$.

The parametric equation of *ab* is

$$\begin{cases} x_{ab} = -\dfrac{d_f}{2}\cos(\pi-\beta) \\ y_{ab} = \dfrac{d_f}{2}\sin(\pi-\beta) \end{cases} \tag{1}$$

where d_f is the diameter of the driven screw root circle, $d_f = R_{st}d_j$, d_j is the pitch diameter, β is the angle parameter, $\beta \in \left[\frac{\pi}{2}, \frac{\pi}{2}+2\tau\right]$, 2τ = 0.16π.

(b) The equation of *bc* is

$$\begin{cases} x_{bc} = R_m \sin\theta \\ y_{bc} = R_m \cos\theta . \end{cases} \tag{2}$$

The relationship between angle θ and R_m is

$$\theta = \arccos\left(\frac{4R_m^{\,2} + d_j^{\,2}\cdot R_{st}(4-R_{st})}{8d_j \cdot R_m}\right) - \arccos\left(1+\frac{d_j^{\,2}R_{st}^{\,2}-R_m^{\,2}}{4d_j^{\,2}(2-R_{st})}\right) \tag{3}$$

where $R_m = \frac{d_j}{2}$. The maximum θ can be expressed as

$$\theta_{\max} = \arccos\left(\frac{4+4R_{st}-R_{st}^{\,2}}{8}\right) - \arccos\left(\frac{7-4R_{st}+R_{st}^{\,2}}{8-4R_{st}}\right) \tag{4}$$

where R_m is the diameter in polar coordinates, $\frac{d_f}{2} \le R_m \le \frac{d_j}{2}$, R_{st} is the root circle coefficient of the driven screw, θ is the angle parameter, $\theta \in \left[\frac{\pi}{2}-\theta_{\max}, \frac{\pi}{2}\right]$.

(c) The modified arc *cd* connects *bc* and *de*. The coordinate of point *o* is

$$\begin{cases} x_o = (\dfrac{d_j}{2}-r)\cos\phi \\ y_o = (\dfrac{d_j}{2}-r)\sin\phi . \end{cases} \tag{5}$$

The parametric equation of *cd* is

$$\begin{cases} x_{cd} = x_o + r\cos t \\ y_{cd} = y_o + r\sin t \end{cases} \tag{6}$$

where r is the radius of *cd*, $\phi = \theta + \left|\arctan\frac{y_f}{x_f}\right|$, ($x_f$, y_f) is the intersection of *bc* and *de*, t is the angle parameter, determined according to radius r and angle ϕ.

(d) The parametric equation of *de* is

$$\begin{cases} x_{de} = \dfrac{d_j}{2}\cos\beta \\ y_{de} = \dfrac{d_j}{2}\sin\beta \end{cases} \tag{7}$$

where β is the angle parameter, $\beta \in \left[2\tau+\theta_{\max}-\frac{\pi}{2}, \frac{\pi}{2}-\theta_{\max}\right]$.

2.2.2 Driving screw profile

As shown in Fig. 4, the profile of the end face of the driving screw includes: tooth root arc *a'b'*, shortened epicycloid *b'c'*, modified arc *c'd'*, and tooth top arc *d'e'*. Parametric equations of each curve are can be derived.

(a) The tooth root arc *a'b'* forms part of the tooth root arc of the driving screw. The curve starts at $\frac{\pi}{2}$ and ends at $\frac{\pi}{2}+2\alpha$.

The parametric equation of *a'b'* is

$$\begin{cases} x_{a'b'} = -\dfrac{d_j}{2}\cos(\pi-\beta) \\ y_{a'b'} = \dfrac{d_j}{2}\sin(\pi-\beta) \end{cases} \tag{8}$$

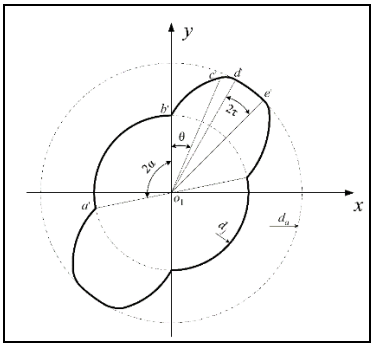

Fig. 4. Cross-sectional profile of driving screw.

where d_j is the pitch diameter, β is the angle parameter, $\beta \in \left[\frac{\pi}{2}, \frac{\pi}{2}+2\alpha\right]$, $\alpha = \frac{\pi}{2} - (\theta_{\max} + \tau)$, 2τ = 0.16π.

(b) The parametric equation of *b′c′* is

$$\begin{cases} x_{b'c'} = R_m \sin\theta \\ y_{b'c'} = R_m \cos\theta \end{cases} \tag{9}$$

The relationship between angle θ and R_m is

$$\theta = \arccos\left(\frac{\frac{5}{4}d_j^{\,2} - R_m^{\,2}}{d_j^{\,2}}\right) - \arccos\left(\frac{\frac{3}{4}d_j^{\,2} + R_m^{\,2}}{d_j^{\,2} \cdot R_m}\right) \tag{10}$$

where $R_m = \frac{d_a}{2} = \frac{d_j}{2} R_{mt}$. The maximum of θ can be determined by

$$\theta_{\max} = \arccos\left(\frac{5 - R_{mt}^{\,2}}{4}\right) - \arccos\left(\frac{3 + R_{mt}^{\,2}}{4R_{mt}}\right) \tag{11}$$

where R_{mt} is the tooth top circle coefficient of the driving screw, R_m is the diameter in polar coordinates, $\frac{d_j}{2} \le R_m \le \frac{d_a}{2}$, θ is the angle parameter, $\theta \in \left[\frac{\pi}{2} - \theta_{\max}, \frac{\pi}{2}\right]$.

(c) The modified arc *c′d′* connects *b′c′* and *d′e′*. The coordinates of point *o* are

$$\begin{cases} x_o = \left(\frac{d_j}{2} R_{mt} - r\right)\cos\phi \\ y_o = \left(\frac{d_j}{2} R_{mt} - r\right)\sin\phi \end{cases} \tag{12}$$

The parametric equation of *c′d′* is

$$\begin{cases} x_{c'd'} = x_o + r\cos t \\ y_{c'd'} = y_o + r\sin t. \end{cases} \tag{13}$$

where *r* is the radius of *c′d′*, $\phi = \theta + \left|\arctan\frac{y_m}{x_m}\right|$, ($x_m$, y_m) is the intersection of *b′c′* and *d′e′*, *t* is the angle parameter, determined according to radius *r* and angle ϕ.

(d) The parametric equation of *d′e′* is

$$\begin{cases} x_{d'e'} = \frac{d_j}{2} R_{mt} \cos\beta \\ y_{d'e'} = \frac{d_j}{2} R_{mt} \sin\beta \end{cases} \tag{14}$$

where β is the angle parameter, $\beta \in \left[\frac{\pi}{2} - \theta_{\max} - 2\tau, \frac{\pi}{2} - \theta_{\max}\right]$.

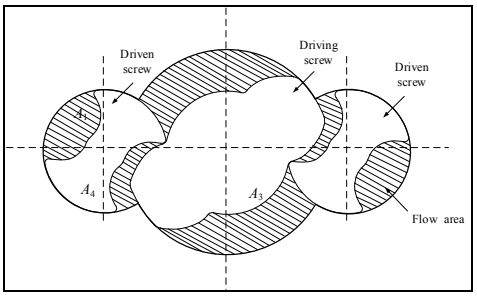

Fig. 5. Flow area of tri-screw pump.

2.3 Theoretical analysis and calculations

As the screws rotate in the tri-screw pump, the flow area between the pump body and the screws gradually increases, starting from zero. Flow area A_1 of the tri-screw pump is the filling area of the working medium in the end face of the tri-screw pump, which is the sum of the shaded areas shown in Fig. 5.

Flow area A_1 can be expressed as

$$A_1 = A_2 - (A_3 + 2 \times A_4) \tag{15}$$

where A_2 represents the area of the three holes on the end face of the pump body, A_3 is the end area of the driving screw, and A_4 is the end area of the driven screw.

Area A_2 of the three holes on the end face of the pump body can be determined from Fig. 5. Then, from Fig. 6, A_2 can be expressed as

$$A_2 = \frac{\pi d_j^{\,2}}{2}(1 + R_{mt}^{\,2}) - 2A_0 \tag{16}$$

where d_j is the pitch circle diameter, R_{mt} is the addendum circle coefficient of the driving screw, and A_0 is the shaded area in Fig. 6. A_0 can be calculated as

$$\begin{aligned} A_0 &= \left(d_a^{\,2} \cdot \beta_1 - d_a^{\,2} \sin\beta_1 \cdot \cos\frac{\beta_1}{2}\right) \\ &+ \left(d_j^{\,2} \cdot \beta_2 - d_j^{\,2} \sin\beta_2 \cdot \cos\frac{\beta_2}{2}\right) \end{aligned} \tag{17}$$

where β_1 and β_2 are the central angles of the left and right arc segments of the shaded area, respectively, $\cos\beta_1 = \frac{d_a - s_1}{d_a}$, $\cos\beta_2 = \frac{d_j - s_2}{d_j}$. For s_1 and s_2, the following expressions can be obtained

$$\begin{cases} (d_j - s_2) + (d_a - s_1) = d_j \\ d_a^{\,2} - (d_a - s_1)^2 = d_j^{\,2} - (d_j - s_2)^2. \end{cases} \tag{18}$$

The end face profiles of the driving screw and of the driven

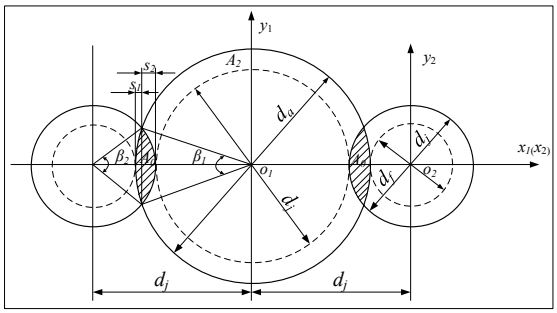

Fig. 6. Hole area of tri-screw pump.

screw are shown in Figs. 3 and 4, respectively. The end face area A_3 of the driving screw is

$$A_3 = d_j^2\left[\int_{\frac{\pi}{2}}^{\frac{\pi}{2}-\alpha}\sin^3\theta\mathrm{d}\theta + R_{mt}^2\cdot\int_0^{\tau}\sin^3\theta\mathrm{d}\theta\right] + \int_{\frac{\pi}{2}-\alpha}^{\frac{\pi}{2}-\alpha-\theta}\int_{\frac{1}{2}d_j}^{\frac{1}{2}d_a} r^2\cos^2\theta\mathrm{d}\theta + \frac{1}{2}r\sin 2\theta\mathrm{d}r. \quad (19)$$

The end face area A_4 of the driven screw is

$$A_4 = d_j^2\left[R_{st}^2\cdot\int_{\frac{\pi}{2}-\tau}^{\frac{\pi}{2}}\sin^3\theta\mathrm{d}\theta + \int_0^{\frac{\beta}{2}}\sin^3\theta\mathrm{d}\theta\right] + \int_{\frac{\pi}{2}-\theta}^{\frac{\pi}{2}}\int_{\frac{1}{2}d_f}^{\frac{1}{2}d_j} r^2\cos^2\theta\mathrm{d}\theta + \frac{1}{2}r\sin 2\theta\mathrm{d}r. \quad (20)$$

2.4 Modeling of driving and driven screws

According to the design requirements presented in Sec. 1.2, the numerical method for calculating the end profile of the driving and driven screws and the meshing relationship is presented in Fig. 7. In zone A, it can be seen that the arc transition occurs in the tooth root of the driving screw, which is in contact with the excessive arc after optimization of the driven screw tip. In zone B, a smooth arc is obtained by optimizing the tooth tip of the driving screw.

The end face geometry was established and the helix line was generated according to the pitch and helix angle. A 3D model of the driving screw and the driven screw were obtained through UG, and geometric parameters of the driving and driven screws structures are listed in Table 2.

Clearance leakage is the main factor involved in pump leakage. As shown in Fig. 8, the leakage of the tri-screw pump is mainly caused by radial clearance, inter-lobe clearance, and side clearance. The radial clearance is the clearance between the tooth top of the screw and the inner wall of the pump cavity, the inter-lobe clearance is between the driving and driven screws in the meshing area, and side clearance between teeth is the normal clearance distributed along the contact line between the screw teeth surfaces in the meshing area. Fluid at the inlet enters a local low-pressure space created by the meshing motion between the screws through the end face. As the screw rotates, the fluid gradually fills this space. Due to clearance, liquid that enters the screw pump by suction is not completely discharged through the outlet, which increases

Table 2. Geometric parameters of driving and driven screw.

	Pitch diameter (mm)	Addendum diameter (mm)	Root diameter (mm)	Lead range (mm)	Length (mm)
Driving screw	45	75	45	75	300
Driven screw	45	45	15	75	300
Centre distance	45	-	-	-	-
Radial clearance	0.1				
Inter-lobe clearance	0.2				

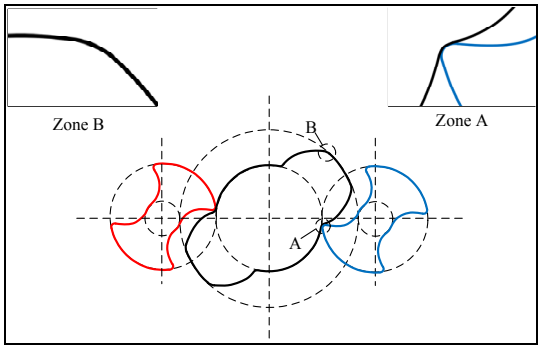

Fig. 7. Tooth profile of screw during end face engagement.

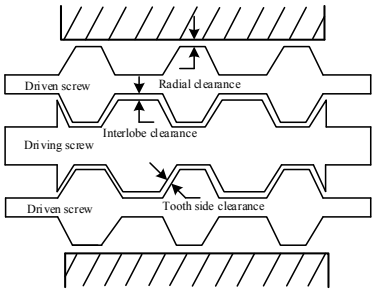

(a)

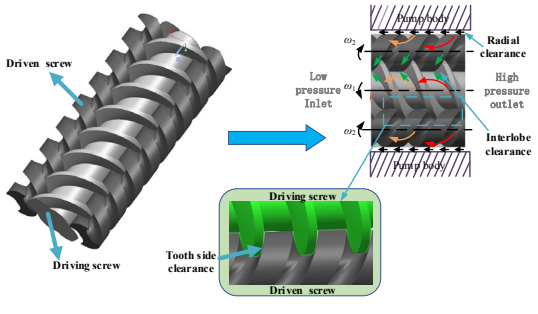

(b)

Fig. 8. Leakage model of tri-screw pump: (a) diagrammatic sketch of leakage clearance of screw pump; (b) clearance in screw pump and leakage paths.

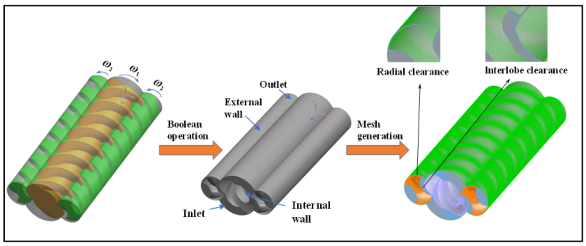

Fig. 9. Flow path model of tri-screw pump.

leakage of the pump, thereby decreasing the volumetric efficiency of the pump.

3. Flow field model of tri-screw pump and boundary conditions

3.1 Flow field model and calculation conditions

Flow characteristics of the tri-screw pump under actual working conditions were studied using CFD in FLUENT 18.1. A screw model was established in the Unigraphics (UG) software, as shown in Fig. 9. The flow channel was modeled with the outer surface of the screw as the inner boundary. A flow field model of the tri-screw pump was established using Boolean operations to combine the solid geometric model with the channel geometric model [24-26]. Due to the complexity of the screw surface, a denser mesh was generated around the screw. A mesh refinement value of 3 was selected in the mesh module. To ensure the boundary was close to the actual model, a polyhedral mesh was generated and imported into FLUENT. There were 1781258 nodes and 411083 elements in the internal flow field grid model of the tri-screw pump.

3.2 Boundary conditions

Due to the complex turbulent flow field in the tri-screw pump, the two-equation renormalized group theory (RNG) k-epsilon (k - ε) turbulence model was used in calculations, and the semi-implicit method for pressure-linked equations (SIMPLE) were used in the tri-screw pump simulations and the convergence accuracy was 10^{-5}. The boundary conditions of the flow field were the inlet and outlet pressure, which were set as 0.1 MPa, and 1-7 MPa, respectively. In addition, hydraulic oil 46 with a density of 890 kg/m^3 and dynamic viscosity of 0.046 Pa·s was selected as the fluid. Considering the actual working conditions and flow characteristics of the fluid medium, the following assumptions can be made [27-30]

(a) The fluid is incompressible.
(b) The flow field is stable.
(c) There is a no-slip boundary at the wall.
(d) The fluid motion is turbulent flow.

According to the basic flow field assumptions listed above, the continuity equation, momentum equation, and structure-equation were defined in Cartesian coordinates as follows [7, 9].

The continuity equation is

$$\frac{\partial \rho}{\partial t}+\frac{\partial(\rho \mu)}{\partial x}+\frac{\partial(\rho v)}{\partial y}+\frac{\partial(\rho w)}{\partial z}=0 . \tag{21}$$

The momentum equation is

$$\begin{cases} \rho \dfrac{\partial \mu}{\partial t}+\nabla \cdot(\rho \mu u)=\nabla(\vartheta grad \mu)-\dfrac{\partial p}{\partial x}+S_{\mu} \\ \rho \dfrac{\partial v}{\partial t}+\nabla \cdot(\rho v u)=\nabla(\vartheta grad v)-\dfrac{\partial p}{\partial y}+S_{v} \\ \rho \dfrac{\partial w}{\partial t}+\nabla \cdot(\rho w u)=\nabla(\vartheta grad w)-\dfrac{\partial p}{\partial z}+S_{w} \end{cases} \tag{22}$$

where ρ is the density, kg/m^3, ∇ is the Hamiltonian operator, u is the velocity vector, μ, v, and w are components of velocity u in the x, y, and z directions, respectively, m/s, ϑ is the kinematic viscosity, m^2/s, p is the static pressure, Pa, S_μ, S_v, and S_w are components of stress in the x, y, and z directions, respectively, in MPa.

By solving the general dynamic equation of classical mechanics, the equation of motion of the structure can be established as

$$\mathrm{M}\overline{\mathrm{Z}}+\mathrm{C}\overline{\mathrm{Y}}+\mathrm{K}\overline{\mathrm{X}}=\mathrm{F}(\mathrm{t}) \tag{23}$$

where M is the mass matrix, C is the damping matrix, K is the stiffness coefficient matrix, $\overline{\mathrm{Z}}$ is the displacement vector, $\overline{\mathrm{Y}}$ is the velocity vector, $\overline{\mathrm{X}}$ is the acceleration vector, F is the force vector, comprised of the gravitational force, centrifugal force, and flow field pressure.

The driving and driven screws rotate in opposite directions at angular velocities of ω_1 and ω_2, respectively, which drives the spiral motion of the fluid in the pump. The velocity of the fluid in the flow path is the same as the fluid velocity on the surface of the screw. The boundary conditions of the flow field were defined as follows:

The velocity of different radiuses on the surface of screw is

$$v_{(\mathrm{r})}=2 \pi r \omega . \tag{24}$$

The velocity of the driving screw is

$$\begin{cases} v_x=-2 \pi \omega_1 y \\ v_y=2 \pi \omega_1 x \\ v_z=0 \end{cases} . \tag{25}$$

The velocity of the driven screw is

$$\begin{cases} v_x=2 \pi \omega_2 y \\ v_y=-2 \pi \omega_2 x \\ v_z=0 \end{cases} \tag{26}$$

Table 3. Results of mesh independence study.

Parameter	1.5 mm	1.2 mm	1 mm	0.8 mm
Total elements	212972	310010	411083	578313
Total nodes	914425	1339858	1781258	2515426
Flow rate (L/min)	118.84	117.43	116.8	114.21

where v_x, v_y, and v_z are components of velocity in the x, y, and z directions, respectively; ω_1 and ω_2 are angular velocities of the driving and driven screws, respectively.

3.3 Grid independence

To verify grid independence, an inter-lobe clearance of 0.1 mm and radial clearance of 0.2 mm were adopted. The outlet pressure was set as 4 MPa and the speed was set to 550 r/min. The mesh size ranged from 0.8 mm to 1.5 mm. The total numbers of elements and nodes as well as the outlet volume flow for different grid sizes are presented in Table 3. The variation of flow rate is relatively small, which verifies the independence of the grid [31].

4. Simulation analysis of flow field

4.1 Velocity field

The flow field inside the tri-screw pump was simulated in Fluent and the results are presented in Fig. 10. From Fig. 10(a), it can be seen that the outer wall velocity is almost zero due to the no-slip boundary condition adopted in the model. As shown in Fig. 10(b), it can be seen that the velocity is concentrated at the screw edges of both the driving and driven screws. The velocity of the driving screw is far greater than that of the driven screw and velocities at the screw edges are greater than those in the screw groove area. Fig. 10(c) shows that the velocity on the top of the screw edge of the driving screw is much larger compared to other areas.

A vortex exists near the screw engagement area due to the pressure difference between the volume of fluid that enters the engagement areas of the driving and driven screws. When the driven screw rotates counterclockwise and the driving screw rotates clockwise, the direction of the fluid changes, creating a vortex. Fig. 10(d) shows that as the screw rotates at high speed, the fluid moves in a circle with the rotation of the screw, and the velocity at the screw edge is relatively large; the velocity at the screw groove is relatively stable and the fluid flows from the inlet to the outlet. Fig. 10(e) shows that the velocity in area A is positive and larger than that in other areas, indicating that the fluid is subjected to positive shear forces and extruded towards the outlet. Positive and negative velocities can be observed in area B. The maximum negative velocity occurs in the area where the spiral groove and meshing area meet and exchange fluid, indicating that leakage will occur between the spiral groove area and pump casing.

When the rotating speed is 500 r/min, flow at the inlet and outlet of the tri-screw pump varies with the angle of the driving screw, as shown in Fig. 11. Since the driving and driven screws have two teeth, the flow rate changes periodically; therefore, for one rotation of the driving screw, two fluctuations in the flow rate can be observed (Fig. 11). The curves of inlet and outlet flow rate change smoothly as the flow fluctuates.

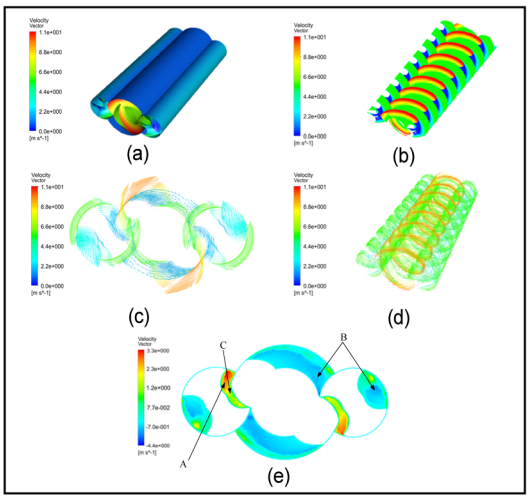

Fig. 10. Velocity field distribution in tri-screw pump: (a) global velocity field; (b) inner wall velocity field; (c) velocity-vector field of inlet surface; (d) velocity-vector field of fluid flow; (e) axial velocity field of inlet surface.

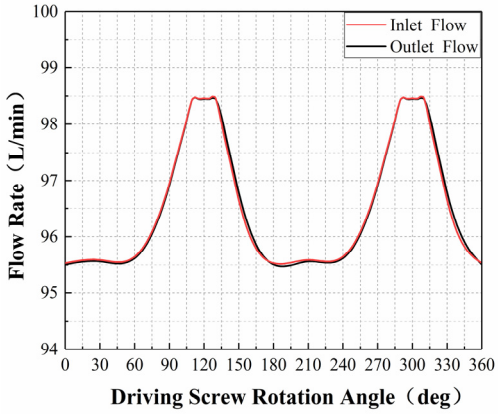

Fig. 11. Curves of flow rate versus screw angle.

4.2 Influence of radial clearance on flow field

Clearance between the screw and the pump body is one of the main causes of internal leakage in the tri-screw pump. Numerical simulations of the internal flow path of pumps with different radial clearances were performed and analyzed. The global pressure contour map for the flow field of the tri-screw pump is shown in Fig. 12(a). The pressure of the tri-screw pump flow path exhibits an obvious step increase between the inlet to the outlet, and the pressure is significantly higher at the screw edge. As shown in Fig. 12(b), there are significant pressure differences between different sections of the pump cavity. Under the same section, the pressure of the driving and the

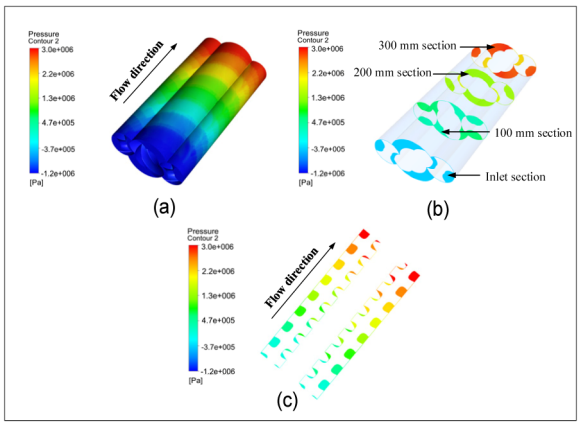

Fig. 12. Pressure field distribution in tri-screw pump: (a) global pressure contour map; (b) pressure in different cross-sectional planes along the axial positions; (c) cross-sectional pressure along flow passage.

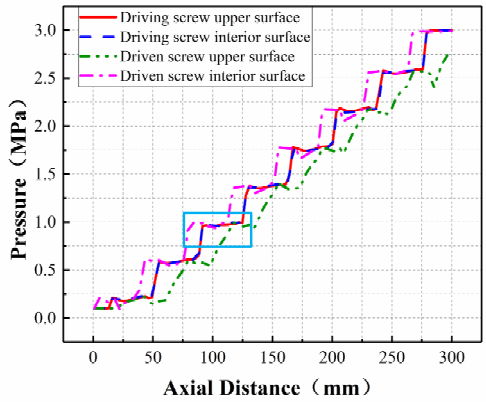

Fig. 13. Pressure along the axial direction in the engagement area.

driven screws are different, which aids fluid flow. Fig. 12(c) shows that the fluid pressure in the middle the engagement area is significantly higher than in other areas.

To clearly observe the pressure distribution in the flow path of the pump, the upper and interior wall surfaces of the flow path were expanded along the axial direction. Step increases in pressure were observed from the low pressure chamber to the high pressure chamber, as shown in Fig. 13. Pressure on the interior wall of the internal flow path is larger than on the upper wall, and the pressure difference between the upper and interior walls aids fluid transmission. In the same pressure chamber, the axial pressure decreases due to leakage.

To observe the influence of radial clearance on the volumetric efficiency of the tri-screw pump, the pressure difference and radial clearance were varied. Pressure differences of 3 MPa, 4 MPa, and 5 MPa were considered. From Fig. 14, it can be seen that as the radial clearance increases, the pressure tends to decrease due to the increase in clearance, which decreases the internal volume of the pump, resulting in leakage. When the radial clearance increases from 0.1 mm to 0.3 mm, the pressure decreases by 16.9 %, 16.6 %, and 15.4 % for pressure differences of 5 MPa, 4 MPa, and 3 MPa, respectively. The

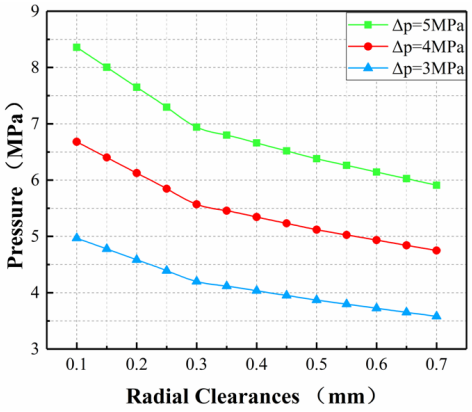

Fig. 14. Curves of pressure versus radial clearance for different pressure differences.

trends illustrated in Fig. 14 suggest that larger pressure differences increase leakage.

4.3 Influence of inter-lobe clearance on flow field

Inter-lobe clearance between the driving and driven screws is an important parameter of the tri-screw pump. To further study the working performance of the tri-screw pump using the given screw profile parameters, the inter-lobe clearance between the driving and driven screws was varied, which changes the pressure difference between the inlet and the outlet. The influence on the pressure field of the tri-screw pump fluid was analyzed.

Pressure differences of 3 MPa, 4 MPa, and 5 MPa were studied. The screw speed was set as 100 r/min, 300 r/min, 500 r/min, or 700 r/min and the inter-lobe clearance was varied from 0-0.5 mm. The relationship between the inter-lobe clearance and the maximum pressure of the flow field is illustrated in Figs. 15 and 16.

As shown in Fig. 15, the maximum pressure in the flow field will also increase as the rotating speed increases. At the same rotating speed, the pressure increased as the inter-lobe clearance increased from 0 mm to 0.1 mm. However, when the clearance was increased from 0.1 mm to 0.5 mm, the pressure began to decrease. When the inter-lobe clearance was 0.1 mm, the maximum pressure was reached. When the rotating speed was 700 r/min and the clearance was increased to 0.2 mm, the pressure decreased by 27.3 %. At rotating speeds of 500 r/min, 300 r/min, and 100 r/min, the pressure decreased by 29.6 %, 28.3 %, and 27.1 %, respectively. Shear stress increased as the rotating speed increase. Moreover, as the inter-lobe clearance increased, the maximum shear stress showed an overall decrease, but stabilized when the clearance values reached 0.35 mm. When the inter-lobe clearance was increased from 0.1 mm to 0.2 mm, the maximum shear stress decreased by 41.7 % at 700 r/min. At 500 r/min, 300 r/min, and 100 r/min, the pressure decreased by 35.4 %, 27.7 %, and 20.4 % respectively.

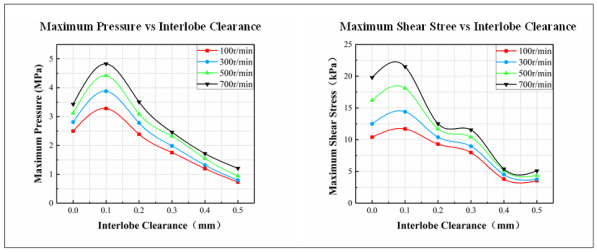

Fig. 15. Curves of pressure and shear stress versus inter-lobe clearance for different rotating speeds.

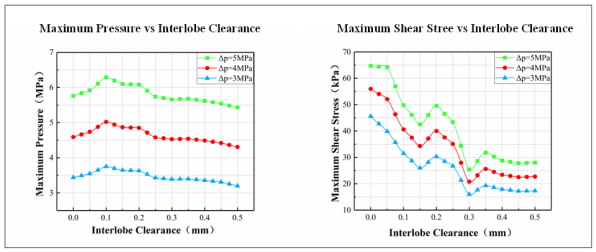

Fig. 16. Curves of pressure and shear stress versus inter-lobe clearance for different pressure differences.

As shown in Fig. 16, the maximum pressure in the flow field will also increase as the pressure difference increases. Under the same pressure difference, the pressure exhibits an upward trend as the inter-lobe clearance increases from 0 mm to 0.1 mm. From 0.1 mm increases to 0.5 mm, the pressure begins to decrease. When the inter-lobe clearance was 0.1 mm, the maximum pressure was reached. When the pressure difference was 5 MPa and the inter-lobe clearance was increased to 0.25 mm, the pressure decreased by 8.7 %. The pressure decreased by 6.1 % and 5.8 %, compared to pressure differences of 4 MPa and 3 MPa, respectively. The reason might be that the excessive inter-lobe clearances affect the volume ratio of the pump and increase leakage in the engagement area. To improve the working performance of the tri-screw pump, the engagement clearance should be reasonably selected during processing and assembly.

As the inter-lobe clearance increased, the maximum shear stress decreased and was stable at inter-lobe clearances above 0.35 mm. When the inter-lobe clearance increased from 0.2 mm to 0.3 mm, the pressure difference was 5 MPa, and the maximum shear stress decreased by 48.79 %. The pressure difference decreased by 48.45 % and 47.12 %, compared with pressure differences of 4 MPa and 3 MPa, respectively.

To analyze the influence of inter-lobe clearance on the flow field, inlet point C was selected as the monitoring point, as shown in Fig. 10(e), and pressure changes at fixed point C were observed under different inter-lobe clearances and inlet and outlet pressure differences. The curve of pressure at point C versus pressure difference is presented in Fig. 17. The pressure at point C remained relatively constant as the pressure difference increased. When the inter-lobe clearance was increased to 0.3 mm, the pressure difference increased, and the

Table 4. Mechanical properties of 38CrMoAl.

Parameter	Value
Density (kg·m^{-3})	7800
Modulus of elasticity (GPa)	210
Poisson's ratio	0.3
Yield strength (MPa)	980
Tensile strength (MPa)	835
Maximum allowable stress (MPa)	557

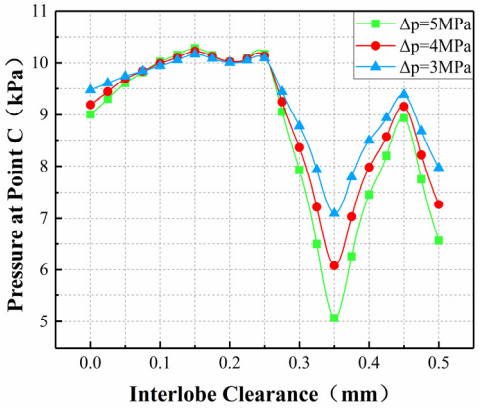

Fig. 17. Curves of pressure at point C versus inter-lobe clearances for various pressure differences.

pressure value also decreased. The curve for the pressure difference of 5 MPa decreased by 36.13 %, compared with the curves for pressure differences of 4 MPa and 3 MPa, which decreased by 27.21 % and 19.21 %, respectively. Under the same pressure difference, the pressure at monitoring point C first increased and then decreased as the inter-lobe clearance was increased, however, the fluctuation was small (0.15-0.25 mm). When the inter-lobe clearance was increased from 0.25 mm to 0.35 mm, there was an obvious decrease in pressure at point C. Above 0.35 mm, the whole body shows a downward trend, suggesting that leakage increases with increasing engagement clearance.

5. Simulation analysis of fluid-structure coupling

5.1 Fluid-structure coupling analysis

When the embedded tri-screw pump is operating, the driving and driven screws are mainly affected by the flow field and torque. Therefore, it is necessary to study the influence of the pressure field, torque, and power on the stress and deformation of the tri-screw pump. To effectively improve the life of the screw, high-strength materials are selected as the driving and driven screw materials. Typically, 38CrMoAl and 38CrMoAl are selected as screw manufacturing materials for their high yield strength and good wear resistance. The mechanical properties of 38CrMoAl are presented in Table 4.

The weak coupling method was used to study fluid-structure

Table 5. Screw deformation at different rotating speeds.

Rotation speed (r/min)	Deformation of driving screw (mm)	Deformation of driven screw (mm)	Maximum equivalent stress (MPa)
500	0.0391	0.0572	329.24
600	0.0310	0.0505	275.23
700	0.0278	0.0485	253.98
800	0.0262	0.0467	238.51
900	0.0253	0.0454	227.17
1000	0.0251	0.0450	219.36
1100	0.0247	0.0448	212.05

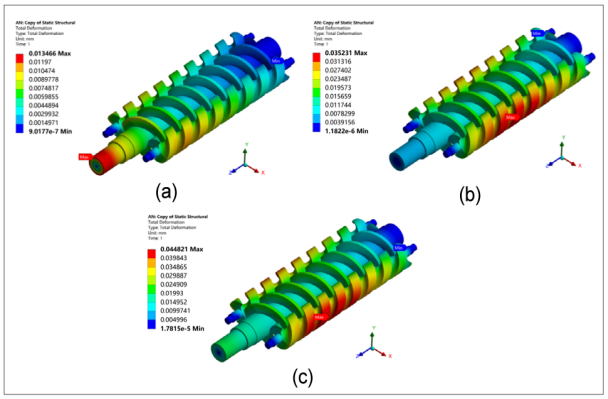

Fig. 18. Deformation of screw under: (a) torque only; (b) pressure only; (c) coupled.

coupling characteristics of the embedded tri-screw pump. First, the pressure distribution of the flow field in the pump was calculated by CFD, then the pressure on the fluid-solid coupling surface was mapped onto the screw structure as the load.

Fig. 18 shows the maximum deformation of screw under the action of torque is 0.0134 mm, under the action of the flow field is 0.0352 mm, and under the coupling effect of torque and flow field is 0.0448 mm; that is, deformation caused by the torque is much less than the deformation caused by the flow field.

For the simulation analysis, the working power of the tri-screw pump was set as 15 kW, and the rotating speed was varied: 500 r/min, 600 r/min, 700 r/min, 800 r/min, 900 r/min, 1000 r/min, and 1100 r/min. The results of fluid-structure coupling analysis are presented in Table 5.

When the rotating speed is 500 r/min, deformation is largest for both the driving screw and the driven screw, and the sum of the deformation is 0.0963 mm, indicating that the designed screw clearance should not be less than 0.0963 mm. The maximum deformation of the driving and driven screws will determine the minimum value of the engagement clearance between the screws. In the actual assembly, the engagement clearance should not be less than the minimum value to avoid friction among the three screws in the pump, and even more serious, sticking. As the rotating speed increases, the total deformation of the screw decreases and the deformation of driving screw and driven screw also decrease. The deformation of the driven screw is always greater than that of driving screw. When the rotating speed is 500 r/min, the equivalent stress of the screw under the coupling effect of flow field pressure and torque is 329.24 MPa, which is far less than the allowable stress of the material (557 MPa), but still meets the strength requirements of the material.

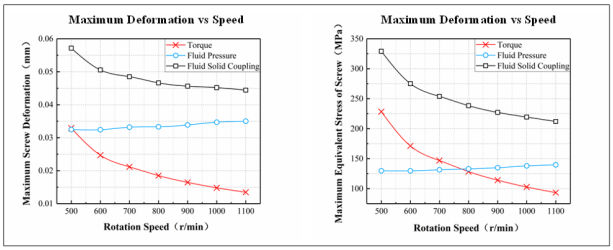

Fig. 19. Curves of deformation and stress versus rotating speed of screw under different working conditions.

5.2 Fluid-structure coupling analysis at different rotating speeds

When the working power of the tri-screw pump is 15 kW, the screw deformation and maximum equivalent stress under torque, flow field pressure, and fluid solid coupling at rotating speeds of 500 r/min, 600 r/min, 700 r/min, 800 r/min, 900 r/min, 1000 r/min, or 1100 r/min are shown in Fig. 19.

Under the torque only condition, the maximum deformation of the screw decreases as the rotating speed increases because when the power of the motor is fixed, the output speed of the motor is inversely proportional to the output torque. That is to say, as the pump speed increases, the input torque of the pump decreases. As the torque applied to the driving and driven screws decreases, the deformation of the screws decreases.

Under the flow field and pressure condition, maximum deformation of the screw increases as the rotating speed increases when the fluid is transported to the outlet at high speed, the reaction force of the fluid increases, deformation of the driving and driven screws increase gradually as the rotating speed increases.

Under the fluid-structure coupling condition, when the rotating speed increases from 500 r/min to 600 r/min, the maximum deformation of the screw decreases by 25 % under torque only and by 11.5 % under fluid-solid coupling. That is to say, deformation caused by torque accounts for a large proportion of the deformation under fluid-solid coupling. When the rotating speed increases from 800 r/min to 1100 r/min, the maximum deformation of the screw decreases by only 2.13 %; that is to say, screw deformation caused by the flow field pressure accounts for a large proportion of the deformation under fluid-solid coupling.

The maximum equivalent stress of the screw under the torque condition decreases as the rotating speed increases, which increases steadily under the flow field pressure condition. Under fluid-structure coupling, the maximum equivalent stress

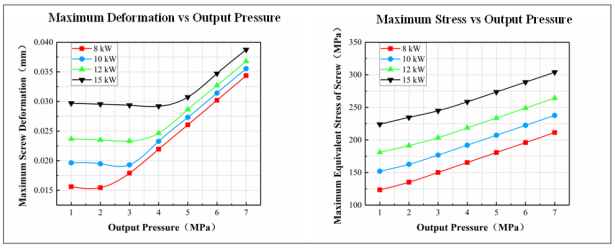

Fig. 20. Curves of deformation and stress in screw versus outlet pressure for different input power.

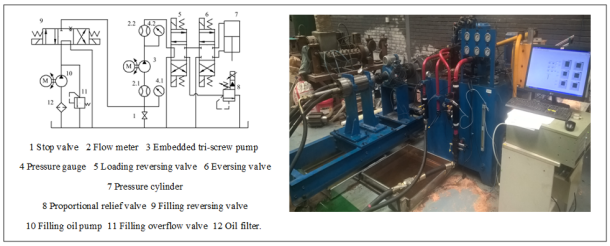

Fig. 21. Experimental setup for measuring embedded tri-screw pump performance.

decreases with as the rotating speed increases. When the rotating speed is between 500 r/min to 600 r/min, the maximum equivalent stress of the screw decreases by 16.4 %. When the rotating speed of the screw is increased to 800 r/min, the maximum equivalent stress decreases by 4.75 %. At this rotating speed, the effect of flow field is stronger than the influence of torque.

5.3 Fluid-structure coupling analysis under different output pressures

Four different output power levels (8 kW, 10 kW, 12 kW, and 15 kW) and seven different output pressures ranging from 1 MPa to 7 MPa were studied. The relationship between maximum deformation and maximum equivalent stress of the screw was simulated under fluid-structure coupling, as shown in Fig. 20.

When the output pressure remains constant, the maximum deformation of the screw increases with increasing input power of the pump (Fig. 20). Under the same input power, the maximum deformation of screw increases with increasing output pressure. When the power is 8 kW and the output pressure is greater than 2 MPa, the maximum deformation of the screw sharply increases; whereas, when the power is 15 kW and the output pressure is greater than 4 MPa, the maximum deformation of the screw sharply increases. This is because the output torque of the motor increases as the input power increases, and the higher the power, the greater the torque effect. When the output pressure is large enough, the effect of flow field pressure on fluid-structure coupling increases, and the influence of torque decreases.

When the output pressure is constant, the maximum equivalent stress of the screw increases as the input power increases. At the same power, the maximum equivalent stress of the screw increases as the output pressure increases. The increasing trends of maximum equivalent stress of the screw produced by the four different input power are similar.

6. Experimental results and analysis

6.1 Experimental setup

To analyze the performance of the embedded tri-screw pump, a prototype was manufactured and a hydraulic test-platform was built. A schematic diagram of the experimental setup and a photo of test bench for the embedded tri-screw pump are presented in Fig. 21.

6.2 Comparative analysis of experimental results

The radial clearance and inter-lobe clearance of the tri-screw pump are the key factors affecting volumetric efficiency. In practice, these two kinds of clearances are affected by many factors, such as machining error, assembly error, fluid pressure, and temperature changes during operation. In the numerical simulation analysis, the clearance size was set according to the theoretical value. By changing the radial clearance and inter-lobe clearance of the screw pump, changes in fluid flow in the pump could be measured.

To study the influence of different clearance values on the flow rate in the pump, the radial clearance was set as 0.2 mm or 0.25 mm, while the inter-lobe clearance was set as 0.1 mm or 0.15 mm: In case 1, the inter-lobe clearance was 0.1 mm and the radial clearance was 0.2 mm; In case 2, the inter-lobe clearance was 0.15 mm and the radial clearance is 0.2 mm; In case 3, the inter-lobe clearance is 0.1 mm and the radial clearance was 0.25 mm. By keeping the rotation speed of the tri-screw pump constant at 450 r/min and changing the load pressure of the tri-screw pump in sequence of 1-7 MPa using the overflow valve, the actual output flow of the tri-screw pump could be measured and compared with the flow calculated in the numerical simulations. In addition, the load pressure was held constant at 4 MPa, the rotating speed of the tri-screw pump was varied in the range of 100-750 r/min, and the actual output flow of the tri-screw pump was measured. The results are presented in Fig. 22.

The results show that when the rotating speed is constant and the inter-lobe clearance increases from 0.1 mm to 0.15 mm, the flow rate of the tri-screw pump decreases by 1.21 % at 1 MPa and 2.75 % at 7 MPa. When the radial clearance increased from 0.2 mm to 0.25 mm, the flow rate decreased by 3.35 % at 1 MPa and 4.92 % at 7 MPa. Comparing the simulation results for case 1 with the experimental data, the difference between the flow rates was 9.03 % at 1 MPa and 3.74 % at 7 MPa.

When the outlet pressure is constant and the inter-lobe clearance increased from 0.1 mm to 0.15 mm, the flow rate of the tri-screw pump decreased by 2.8 % at 100 r/min and

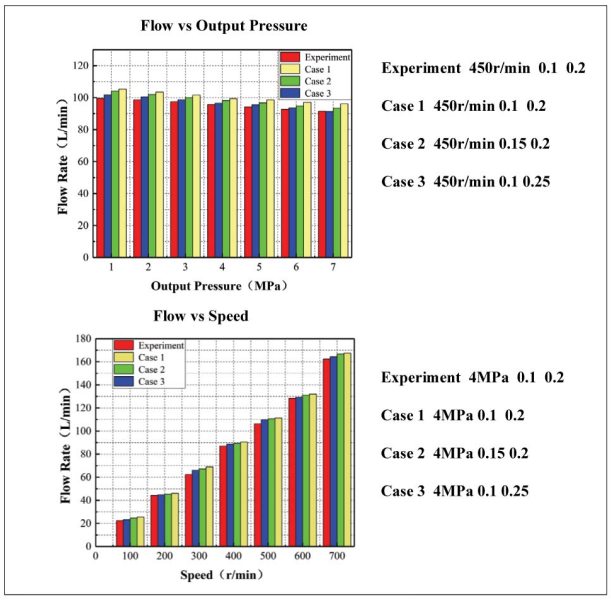

Fig. 22. Curves of flow rate versus rotating speed and output pressure for different screw clearances.

0.52 % at 750 r/min. When the radial clearance was increased from 0.2 mm to 0.25 mm, the flow rate decreased by 5.7 % at 100 r/min and 1.4 % at 750 r/min. Comparing the simulation results for case 1 with the experimental data, the difference in flow rate was 1.15 % at 100 r/min and 3.13 % at 750 r/min.

Through the above analysis, it was found that as the outlet pressure of the tri-screw pump increases, the flow rate gradually decreases; whereas, the increase in rotating speed of the tri-screw pump increases the flow rate. Under the same conditions, simulation values were slightly higher than the experimental values, but the differences in flow rate values were less than 10 %. Trends observed in experimental results and simulation results were consistent.

7. Conclusions

This paper presented a new embedded tri-screw servo motor pump. Theoretical calculations and finite element simulations were used to study the internal flow field and changes in fluid pressure and flow in the pump. The simulation results were verified by experimental data and provide a theoretical basis for follow-up studies of the embedded tri-screw pump. The main conclusions of this work can be summarized as follows:

1) Profiles of the end face of the driving and driven screw teeth were derived, and parametric equations were obtained for the blunt end of the driving and driven screw. Contact points of the driving and driven screws move inward, reducing wear between the driving and driven screw teeth.

2) The velocity and pressure distributions of the internal flow field of the tri-screw pump were obtained through simulations. Radial and inter-lobe clearances were shown to have an influence on the pressure and speed of fluid flow in the tri-screw pump. When the radial clearance increased from 0.1 mm to 0.3 mm, the pressure decreased by 16.9 %, 16.6 %, and 15.4 % for pressure differences of 5 MPa, 4 MPa, and 3 MPa, respectively. When the radial clearance was increased, the pressure in the pump decreased. By varying the inter-lobe clearance and pressure difference between the inlet and outlet of the screw, the maximum pressure in the pump was first found to increase then decrease with increasing inter-lobe clearance. When the inter-lobe clearance was 0.1 mm, the maximum pressure was reached. When the pressure difference was 5 MPa and the inter-lobe clearance was increased to 0.25 mm, the pressure decreased by 8.7 %. The pressure decreased by 6.1 % and 5.8 % with pressure differences of 4 MPa and 3 MPa, respectively. In addition, shear stress decreased as the inter-lobe clearance was increased.

3) Coupling of power, screw speed, channel pressure, torque, and other factors of the tri-screw pump were shown to influence the deformation of the driving and driven screws. When the rotating speed of the tri-screw pump is 500 r/min, the inter-lobe clearance of the screw will not be lower than 0.0963 mm. Deformation and stress in the driving and driven screws are mainly caused by coupling of torque and fluid pressure under different working conditions. As the screw speed increases, the influence of torque on screw deformation and stress decreases, and the influence of fluid pressure ratio increases. When the output pressure is constant, the maximum deformation and the maximum equivalent stress of the screw are proportional to the power. When the power is fixed, the maximum deformation and the maximum equivalent stress of the screw are proportional to the output pressure.

4) The results of experiments performed on a prototype were compared to the simulation data. As outlet pressure in the tri-screw pump increases, the flow rate gradually decreases; whereas, increasing the rotating speed of the tri-screw pump increases the flow rate increases. The simulation value was slightly higher than the experimental values under the same conditions, and differences in flow rates were less than 10 %. According to the clearance calculations, more leakage is caused by radial clearance, which can more easily affect the volumetric efficiency of the pump. The results provide a reference for the structural design and optimization of tri-screw pumps.

Acknowledgments

The author(s) disclosed receipt of the following financial support for the research, authorship, and/or publication of this article: This work was supported by the Natural Science Foundation of Shaanxi Province of China (Grant No. 2019JM-466), and Talent Launch Plan Project of Shaanxi University of Technology (Grant No. SLGQD1811).

Nomenclature

d_j : Pitch circle diameter of driving and driven screws
R_{st} : The root circle coefficient of driven screw

R_{mt} : The tooth top circle coefficient of the driving screw
x_f, y_f : The intersection of *bc* and *de*
x_m, y_m : The intersection of *b'c'* and *d'e'*
t : The angle parameter
ρ : The density
∇ : The Hamiltonian operator
μ, v, w : The components of velocity u in the x, y, and z directions
p : The static pressure
S_μ, S_v, S_w : The components of stress in the x, y, and z directions
ϑ : The kinematic viscosity
ω_1, ω_2 : The angular velocities of the driving and driven screws
v_x, v_y, v_z : The components of velocity in the x, y, and z directions
A_1 : Flow area A_1
A_2 : The area of the three holes on the end face of the pump body
A_3 : The end area of the driving screw
A_4 : The end area of the driven screw

References

[1] Q. Tang and Y. Zhang, Screw optimization for performance enhancement of a twin-screw pump, *P. I. Mech. Eng. E.-J. Pro.,* 228 (2013) 73-84.

[2] Q. Tang, Y. Zhang, L. Pei and J. Tang, Optimal design of screw and flow field analysis for twin-screw pump, *ASME 2011 International Design Engineering Technical Conferences and Computers and Information in Engineering Conference: American Society of Mechanical Engineers* (2011) 593-600.

[3] D. Yan, A. Kovacevic, Q. Tang, S. Rane and W. Zhang, Numerical modelling of twin-screw pumps based on computational fluid dynamics, *Proc. IMechE, Part C: J. Mechanical Engineering Science* (2016) 231.

[4] T.-Y. Gao, D.-F. Yang, F. Cao and J.-C. Jiao, Temperature and thermodynamic deformation analysis of the rotors on a twin screw multiphase pump with high gas volume fractions, *Journal of Zhejiang University-Science A,* 12 (2011) 720-730.

[5] K. Rabiger, T. M. A. Maksoud, J. Ward and G. Hausmann, Theoretical and experimental analysis of a multiphase screw pump, handling gas-liquid mixtures with very high gas volume fractions, *Exp. Therm. Fluid. Sci.,* 32 (2008) 1694-1701.

[6] K. Syzrantseva and V. Syzrantsev, Load on multipair contact zones of operating parts of screw pumps and motors: a computer analysis, *Procedia Engineering,* 150 (2016) 768-774.

[7] S. Rane, A. Kovacevic, N. Stosic and M. Kethidi, Grid deformation strategies for CFD analysis of screw compressors, *Int. J. Refrig.,* 36 (2013) 1883-1893.

[8] S. Rane, A. Kovacevic, N. Stosic and M. Kethidi, Deforming grid generation and CFD analysis of variable geometry screw compressors, *Computers & Fluids,* 99 (2014) 124-141.

[9] S. Rane, A. Kovačević and N. Stošić, Analytical grid generation for accurate representation of clearances in CFD for screw machines, *IOP Conference Series: Materials Science and Engineering,* 90 (2015) 012008.

[10] Z. H. Fong and F. C. Huang, Evaluating the interlobe clearance and determining the sizes and shapes of all the leakage paths for twin-screw vacuum pump, *Proc. IMechE, Part C: J. Mechanical Engineering Science,* 220 (2006) 499-506.

[11] H. Ding, Y. Jiang and S. Dhar, CFD modelling of coupled heat transfer between solid and fluid in a twin screw compressor, *IOP Conference Series: Materials Science and Engineering,* 604 (2019) 012005.

[12] T. N. Mustafin, R. R. Yakupova, A. V. Burmistrova, M. S. Khamidullina and I. G. Khisameeva, Analysis of influence of screw compressor construction parameters and working condition on rotor temperature fields, *Procedia Engineering,* 152 (2016) 423-433.

[13] I. Papes, J. Degroote and J. Vierendeels, New insights in twin screw expander performance for small scale ORC systems from 3D CFD analysis, *Appl. Therm. Eng.,* 91 (2015) 535-546.

[14] D. Rowinski, A. Nikolov and A. Brümmer, Modeling a dry running twin-screw expander using a coupled thermal-fluid solver with automatic mesh generation, *IOP Conference Series: Materials Science and Engineering,* 425 (2018) 12-19.

[15] J. Wei, Q. Sun, X. Sun and W. Sun, A study on rotor profile design for a novel twin-screw kneader, *International Jounal of Precision Engineering and Manufacturing,* 14 (2013) 451-459.

[16] J. Wei, Rotor profiles design method and numerical simulation for twin-screw kneader, *J. Mech. Eng.,* 49 (2013) 63.

[17] S. R. Prashanth et al., CFD modelling and performance analysis of a twin screw hydrogen extruder, *Fusion Eng. Des.,* 138 (2019) 151-158.

[18] F. Li, *Screw Pump*, Beijing, China: Machine Press (2010).

[19] J. Xu, Q. Feng and W. Wu, Geometrical design and investigation of a new profile of the three screw pump, *J. Mech. Design,* 133 (2011) 094501.

[20] Z.-J. Liu, Y.-C. Zhao, Z.-Q. Gan and D.-L. Hui, Driving shaft fatigue optimization design of Ω type profile twin-screw pumps, *J. Mech. Sci. Technol.,* 32 (2018) 5089-5096.

[21] A. Lyashkov and K. Panchuk, Computer modeling of a pump screw and disc tool cross shaping process, *Procedia Engineering,* 113 (2015) 174-180.

[22] Z. Liu, Q. Tang, N. Liu and J. Song, A profile error compensation method in precision grinding of screw rotors, *Int. J. Adv. Manuf. Tech.,* 100 (2018) 2557-2567.

[23] Z. Liu, Q. Tang, Y. F. Zhang and N. Liu, An analytical method for surface roughness prediction in precision grinding of screw rotors, *Int. J. Adv. Manuf. Tech.,* 103 (2019) 2665-2676.

[24] Y.-Q. Zhao et al., Determining the repair width and CNC grinding of screws of triple-screw pump, *Int. J. Adv. Manuf. Technol.*, 97 (1-4) (2018) 389-400.

[25] Y.-Q. Zhao et al., Design and simulation of AC servo three-screw motor pump, *IEEE International Conference on Aircraft Utility Systems* (2016) 254-265.

[26] P. Dong, S. Zhao, Y. Zhao, P. Zhang and Y. Wang, Design and experimental analysis of end face profile of tri-screw pump, *Proceedings of the Institution of Mechanical Engineers, Part A: J. of Power and Energy,* 234 (2019) 481-489.

[27] H. Lee, K. Park and H. Choi, Experimental investigation of tip-leakage flow in an axial flow fan at various flow rates, *J. of Me-*

chanical Science and Technology, 33 (2019) 1271-1278.
[28] Y.-I. Kim, S. Kim, H.-M. Yang, K.-Y. Lee and Y.-S. Choi, Analysis of internal flow and cavitation characteristics for a mixed-flow pump with various blade thickness effects, *J. of Mechanical Science and Technology,* 33 (2019) 3333-3344.
[29] S. E. Lim and C. H. Sohn, CFD analysis of performance change in accordance with inner surface roughness of a double-entry centrifugal pump, *J. of Mechanical Science and Technology,* 32 (2018) 697-702.
[30] S. Kim, U.-B. Jeong, K.-Y. Lee, J.-H. Kim, J.-Y. Yoon and Y.-S. Choi, Design optimization of mixed-flow pump impellers with various shaft diameters at the same specific speed, *J. of Mechanical Science and Technology,* 32 (2018) 1171-1180.
[31] M. Zhu et al., Computational fluid dynamics and experimental analysis on flow rate and torques of a servo direct drive rotary control valve, *Proc IMechE, Part C: J. Mechanical Engineering Science* (2018).

Yongqiang Zhao received his B.S. degree from Shaanxi University of Technology, China, in 2000, and his M.S. and Ph.D. degrees from School of Mechanical Engineering, Xi'an Jiaotong University, China, in 2007 and 2017, respectively. He is currently a Professor at School of Mechanical Engineering, Shaanxi University of Technology, China. His research interests are in fluid transmission and control, special manufacturing process and equipment, computer control of mechanical-electrical-hydraulic system, etc.

Bowen Zhu received his B.S. degree from Chongqing University of Arts and Science, China, in 2018. He is currently a student and studying for a M.S. degree at School of Mechanical Engineering, Shaanxi University of Technology, China. His research interests are in fluid transmission and control, and computer control of mechanical-electrical-hydraulic system, etc.

Hongling Hou received her B.S. degree from Shaanxi University of Technology, China, in 2000, and her M.S. degree from Xi'an Jiaotong University, China, in 2006. She is currently an Associate Professor at School of Mechanical Engineering, Shaanxi University of Technology, China. Her research interests are in advanced manufacturing technology and equipment, fluid transmission and control, etc.

Shengdun Zhao received his B.S., M.S. and Ph.D. from Xi'an Jiaotong University, China, in 1983, 1986 and 1997, respectively. His currently a Professor at School of Mechanical Engineering, Xi'an Jiaotong University, China. His research interests are in plastic forming technology and equipment, computer control of mechanical-electrical-hydraulic system, fluid transmission and control, etc.